Xu, Q., Zhao, J., Yuan, X., Liu, H., Pei, S. (2017): Detailed Configuration of the Underthrusting Indian Lithosphere Beneath Western Tibet Revealed by Receiver Function Images. - *Journal of Geophysical Research*, *122*, 10, pp. 8257—8269.

DOI: http://doi.org/10.1002/2017JB014490

AGU PUBLICATIONS

JGR

Journal of Geophysical Research: Solid Earth

RESEARCH ARTICLE
10.1002/2017JB014490

Key Points:
- An intracrustal discontinuity is observed at ~55 km depth representing the upper border of the underthrusting Indian lower crust
- The midcrustal low-velocity zone at ~20 km depth is clearly visible, which reflects the presence of partially melt crust
- The LAB images indicate that the Indian lithospheric mantle is underthrusting beneath the southern Tibet with ramp-flat shape

Supporting Information:
- Supporting Information S1

Correspondence to:
Q. Xu,
xuqiang@itpcas.ac.cn

Citation:
Xu, Q., Zhao, J., Yuan, X., Liu, H., & Pei, S. (2017). Detailed configuration of the underthrusting Indian lithosphere beneath western Tibet revealed by receiver function images. *Journal of Geophysical Research: Solid Earth*, *122*, 8257–8269. https://doi.org/10.1002/2017JB014490

Received 1 JUN 2017
Accepted 13 OCT 2017
Accepted article online 18 OCT 2017
Published online 28 OCT 2017

Detailed Configuration of the Underthrusting Indian Lithosphere Beneath Western Tibet Revealed by Receiver Function Images

Qiang Xu[1,2], Junmeng Zhao[1,2], Xiaohui Yuan[3], Hongbing Liu[1,2], and Shunping Pei[1]

[1]Key Laboratory of Continental Collision and Plateau Uplift, Institute of Tibetan Plateau Research, Chinese Academy of Sciences, Beijing, China, [2]CAS Center for Excellence in Tibetan Plateau Earth Sciences, Beijing, China, [3]Deutsches GeoForschungsZentrum GFZ, Potsdam, Germany

Abstract We analyze the teleseismic waveform data recorded by 42 temporary stations from the Y2 and ANTILOPE-1 arrays using the *P* and *S* receiver function techniques to investigate the lithospheric structure beneath western Tibet. The Moho is reliably identified as a prominent feature at depths of 55–82 km in the stacked traces and in depth migrated images. It has a concave shape and reaches the deepest location at about 80 km north of the Indus-Yarlung suture (IYS). An intracrustal discontinuity is observed at ~55 km depth below the southern Lhasa terrane, which could represent the upper border of the eclogitized underthrusting Indian lower crust. Underthrusting of the Indian crust has been widely observed beneath the Lhasa terrane and correlates well with the Bouguer gravity low, suggesting that the gravity anomalies in the Lhasa terrane are induced by topography of the Moho. At ~20 km depth, a midcrustal low-velocity zone (LVZ) is observed beneath the Tethyan Himalaya and southern Lhasa terrane, suggesting a layer of partial melts that decouples the thrust/fold deformation of the upper crust from the shortening and underthrusting in the lower crust. The *Sp* conversions at the lithosphere-asthenosphere boundary (LAB) can be recognized at depths of 130–200 km, showing that the Indian lithospheric mantle is underthrusting with a ramp-flat shape beneath southern Tibet and probably is detached from the lower crust immediately under the IYS. Our observations reconstruct the configuration of the underthrusting Indian lithosphere and indicate significant along strike variations.

1. Introduction

The continued convergence between India and Eurasia since their initial collision at 50–65 Ma has led to the formation of the Tibetan Plateau (DeCelles et al., 2002; Ding et al., 2005; Yin & Harrison, 2000). This raises a question, how the lithospheric deformation beneath Tibetan Plateau is linked to the >2,000 km of postcollision consumed lithosphere (van Hinsbergen et al., 2011). To address this fundamental problem, several seismic experiments have been conducted in the central and eastern Tibetan Plateau, including INDEPTH (Kind et al., 2002; Nelson et al., 1996; Zhao et al., 1993), Hi-CLIMB (Nabelek et al., 2009), ANTILOPE (Zhao et al., 2010, 2014), and HIMNT (Schulte-Pelkum et al., 2005) which have increased our knowledge of the lithospheric structure and geodynamic processes. Seismic images suggest that the Indian crust is underthrusting beneath the Himalaya along the Main Himalayan Thrust (MHT) acting as a decollement layer (Caldwell et al., 2013; Zhao et al., 1993) and continues to extend beneath the central Lhasa terrane (Schulte-Pelkum et al., 2005; Shi et al., 2015; Zhang et al., 2014). During the plate convergence, the Indian upper crust has been partially transferred into the Himalaya through either crustal-scale thrust duplexing (Gao et al., 2016) or midcrustal channel flow (Beaumont et al., 2001). Receiver function images along the ANTILOPE-II linear array at ~86°E clearly show that the MHT is linked to an intracrustal interface at ~60 km beneath the Lhasa terrane, namely, the Moho doublet, and marks the upper border of the underthrusting Indian crust (Xu et al., 2015). However, it is unclear whether such underthrusting pattern of the Indian lower crust is applicable for western Tibet (Gilligan et al., 2015; Razi, Levin, Roecker, & Gilligan, 2014).

There is no consensus on the geometry of the underthrusting Indian lithospheric mantle beneath western Tibet. Tomographic images indicate that the fast Indian lithosphere mantle has extended subhorizontally to the Jinsha River suture (JRS) along the ANTILOPE-I profile at ~82°E (Li et al., 2008; Zhao et al., 2014), consistent with the results of surface wave tomography (Maurya et al., 2016). However, this feature is different from the ramp-flat geometry of the underthrusting Indian lithospheric mantle that has been imaged by *S*

receiver functions (Zhao et al., 2010), and the transformation from underthrusting to drip in the Indian lithospheric mantle (Razi et al., 2016). Furthermore, the shapes of the underthrusting Indian lithospheric mantle from west to east exhibit clear along strike variations (Li et al., 2008; Liang et al., 2016; Shi et al., 2015; Xu et al., 2011).

The depth of the Moho in western Tibet is still debated. At 79–82°E, the Moho deepens northward from ~50 km beneath the Himalaya (Caldwell et al., 2013) to 70–90 km beneath the Lhasa and Qiangtang terranes with a Moho offset of ~12 km observed at the Bangong-Nujiang suture (BNS) (Rai et al., 2006; Wittlinger et al., 2004). Based on H-κ stacking, the Moho is observed to be segmented along ~80°E by major subvertical faults (Zhang et al., 2014). In contrast, results from the joint inversion of *P* receiver functions and Rayleigh wave group velocity dispersion indicate that no significant offsets exist in the Moho depth other than a ~20–30 km step across the Altyn-Tagh fault (Gilligan et al., 2015).

Midcrustal low-velocity zones (LVZs) at depths of 15–40 km have been widely observed in the eastern Tibetan Plateau using diverse geophysical methods, including active source seismic experiments (Brown et al., 1996; Nelson et al., 1996), ambient noise tomography (Yang et al., 2012), and receiver functions (Xu et al., 2015). These midcrustal LVZs coincide with high-conductivity (low resistivity) zones that have been identified by magnetotelluric (MT) studies (Wei et al., 2001). They are generally considered to be caused by the presence of partial melt and/or aqueous fluids and provide the necessary conditions for the occurrence of channel flow (Beaumont et al., 2001). However, several studies have shown that these LVZs are discontinuous and located at different depths (Hetenyi et al., 2011; Xu et al., 2013). Regional tomographic images do not confirm the existence of LVZs in the middle crust in our study region (Razi, Levin, Roecker, & Gilligan, 2014). Thus, the spatial interconnection of these LVZs and the feasibility of the channel flow model are still open for discussion.

This paper explores the Moho, the intracrustal interface, the midcrustal LVZs, and the lithosphere-asthenosphere boundary (LAB) beneath western Tibet using *P* and *S* receiver function (P-RF and S-RF)]techniques. Our results reveal a detailed geometry of the underthrusting Indian lithosphere and help to identify the mechanisms of the lithosphere deformation across western Tibet.

2. Data

The seismic waveform data that we used in this study were recorded by two experiments in western Tibet (Figure 1). The seismic stations cover the Tethyan Himalaya and Lhasa terranes, which are separated by the Indus-Yarlung suture (IYS). The Y2 array, consisted of 30 Streckeisen STS-2 seismometers and Quanterra Q330 digitizers, was operated from July 2007 to May 2011 (Razi, Levin, Roecker, & Gilligan, 2014). A north-south trending linear array, entitled ANTILOPE-1 (the first stage of the Array Network of Tibetan International Lithospheric Observation and Probe Experiments), was operated between 2006 and 2007 by the geophysical group of the Institute of Tibetan Plateau Research, Chinese Academy of Science (ITPCAS) (Zhao et al., 2014). In this study, 12 broadband stations from the southern part of the ANTILOPE-1 profile, equipped with CMG-3ESP sensors and RefTek 130 data acquisition systems at a sample rate of 40 samples-per-second, are used to fill the station gaps of the Y2 array (Figure 1).

For the P-RF calculations, we extracted the *P* wave waveforms for earthquakes from the USGS earthquake catalog with magnitudes larger than 5.5 Mb and at epicentral distances between 30° and 95°. For the S-RF analysis, we used the teleseismic earthquakes with magnitude larger than 5.5 Mb and the *S* and SKS- wave (*S* phases) waveforms at epicentral distances of 60°–85° and 85°–120°, respectively. The epicenters of all the distant earthquakes used in calculating P-RFs and S-RFs are shown in Figure 2. Prior to any other processing steps, all the seismograms are filtered with a band-pass filter of 1–50 s. We then visually checked all of the three-component waveforms and selected events with high signal-to-noise ratios as well as clear *P*- and *S*-phase arrivals for further processing.

3. Methodology

The P-RF method employs the *P*-to-*s* (*Ps*) converted waves originating from seismic impedance contrasts to investigate the velocity discontinuities in the crust and upper mantle, while the S-RF method utilizes the *S*- and SKS-to-p (*Sp*) conversions. P-RFs are useful for studying discontinuities in the crust and mantle

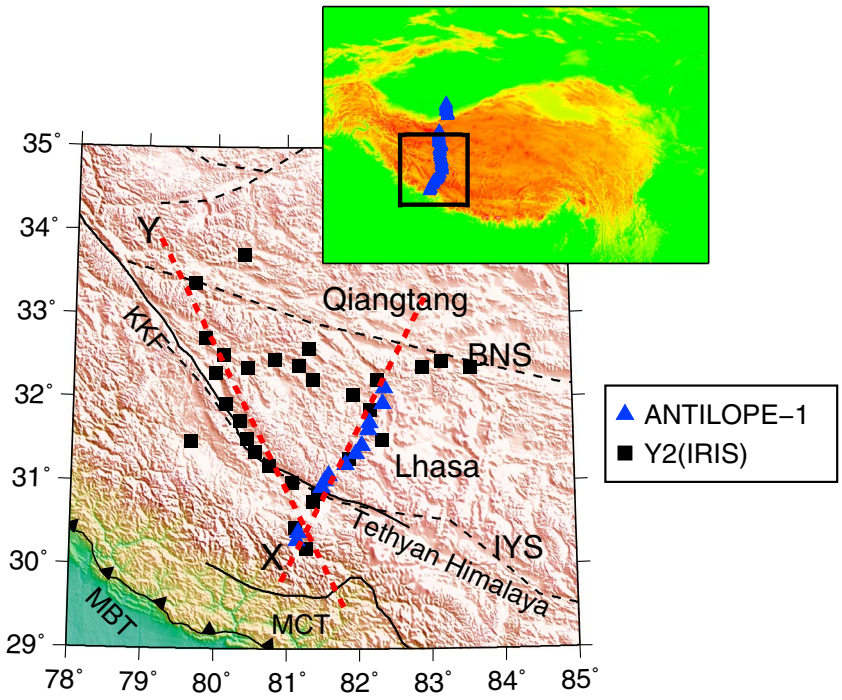

Figure 1. Topographic map showing the locations of the seismic stations used in this study. The blue triangles are the stations from the ANTILOPE-1 project, while the stations from the IRIS Y2 array are shown as black squares. The red dashed lines indicate the locations of profiles X and Y, which were used for depth migration. Black rectangle in the top right inset shows the corresponding locations of the study region in the Tibetan Plateau. The abbreviations are IYS, Indus-Yarlung suture; BNS, Bangong-Nujiang suture; MBT, Main Boundary Thrust; MCT, Main Central Thrust; and KKF, Karakoram fault.

transition zones; however, the *Ps* conversions at mantle lithospheric depths are generally difficult to identify on P-RFs since they are mostly hindered by the significant reverberations from other possible intracrustal discontinuities. In contrast, S-RFs have the advantage of being free of the influence of crustal multiples, because *Sp* conversions and crustal multiples arrive on the opposite sides of the direct *S* or SKS phases, and, therefore, are automatically separated from each other (Kumar & Kawakatsu, 2011). Consequently, S-RFs and P-RFs have become complementary tools for imaging seismic discontinuities in different tectonic regions.

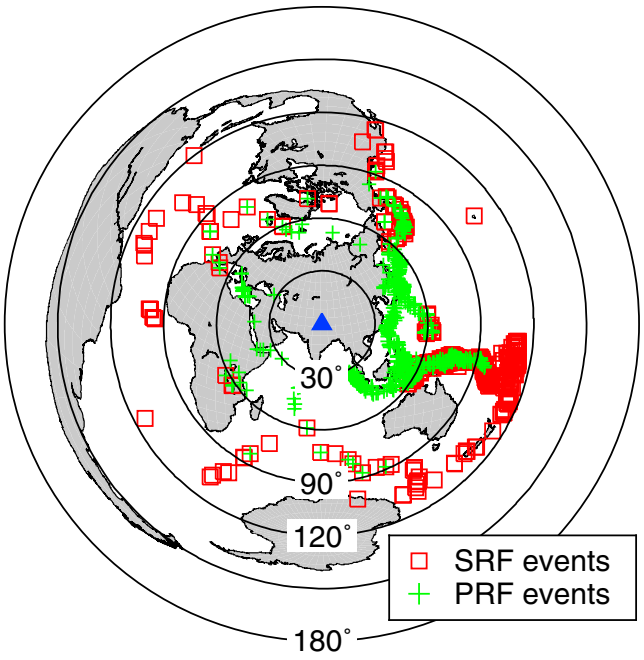

Figure 2. Epicental distribution of the teleseismic events used for the P-RF and S-RF analyses. The blue triangle marks approximately the center of our study area.

3.1. Receiver Function Calculation

The procedures for computing the receiver functions mainly consist of coordinate rotation and deconvolution (Kind et al., 2012; Yuan et al., 2006). First, we rotate the three-component seismograms (ZNE) into a ray-based coordinate system (LQT) that corresponds to the P-SV-SH components. For P-RF calculation, we use theoretical back azimuth and incidence angle. For S-RF, to clearly isolate the P-SV-SH components, we choose an optimized incidence angle, with which the amplitudes within a time window of ±1 s around the *S* phases arrival on the *P* component will be minimized by rotation. Second, we use a spiking deconvolution in the time domain as a source normalization procedure to remove the effects of the source and propagation path (Yuan et al., 1997). A P-RF is thus obtained by deconvolving the *P* from the SV component, and an S-RF is a result of deconvolving the SV from the *P* component. Since *Ps* conversions arrive in *P* wave coda, whereas *Sp* conversions are precursors to *S*, and an *Sp* conversion from the same discontinuity has an

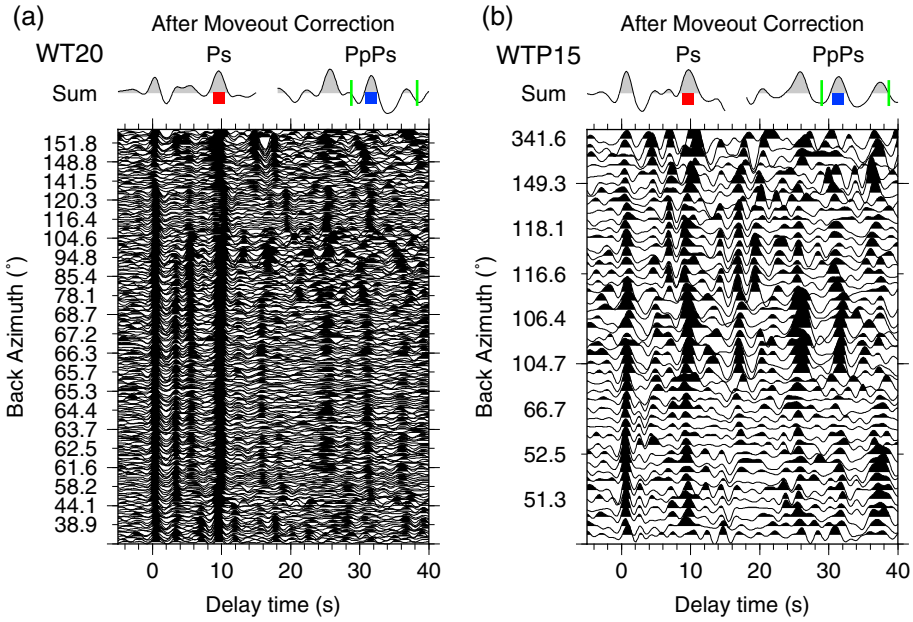

Figure 3. Examples of stations WT20 (Y2) and WTP15 (ANTILOPE-1) showing the individual P-RFs sorted by back azimuth (bottom) and the sum traces (top) after moveout corrections for *Ps* and PpPs, respectively. The red and blue squares mark the picked arrival times of the Moho *Ps* and PpPs conversions, respectively. The green ticks label the time window of Moho PpPs conversion appearance predicted by two V_p/V_s ratios of 1.6 and 2.0 combined with the picked Moho *Ps* delay time.

opposite sign as that of a *Ps* conversion, the additional steps in the S-RF processing are to reverse the time axis and to change the sign of amplitudes, so that S-RF can be directly compared with P-RF. At last, we produce 5685 P-RFs and 2306 S-RFs in total.

3.2. The Moho Depth and V_p/V_s Ratio

Under the assumption of a homogeneous crust, the delay times for the Moho *Ps* and PpPs can be expressed as follows:

$$t_{Ps} = h\left(\sqrt{V_s^{-2} - p^2} - \sqrt{V_p^{-2} - p^2}\right)$$

$$t_{PpPs} = h\left(\sqrt{V_s^{-2} - p^2} + \sqrt{V_p^{-2} - p^2}\right),$$

where h is the Moho depth, p is the reference slowness, and V_p and V_s are the average crustal velocities of *P* and *S* waves. Therefore, the h and V_p/V_s ratio can be calculated by (Li & Yuan, 2003; Yuan et al., 2002)

$$h = \left(t_{PpPs} - t_{Ps}\right)/2\sqrt{V_p^{-2} - p^2}$$

$$V_p/V_s = \sqrt{A^2 - \left(A^2 - 1\right)p^2V_p^2}$$

where $A = (t_{PpPs} + t_{Ps})/(t_{PpPs} - t_{Ps})$.

We stack P-RFs for each station for two separate time windows encompassing the *Ps* and PpPs crustal multiple phases, respectively. Before the summation, all of the P-RFs are moveout corrected to a reference slowness of 6.4 s/° (corresponding to a reference epicentral distance of 67°) for the *Ps* and PpPs, respectively. Based on the available Moho depths beneath western Tibet, the Moho *Ps* conversion appears in a time window of 5–12 s, which can be taken as the reference for picking the Moho *Ps* phase. We then pick the Moho PpPs phase at each station within a short time window predicted by the corresponding Moho *Ps* delay time and two V_p/V_s ratios of 1.6 and 2.0. Figure 3 clearly indicates two examples of picking Moho *Ps* and PpPs phases at adjacent stations WT20 and WTP15, which belong to Y2 array and ANTILOPE-1 profile, respectively. The appearance of P-RFs and the delay times of the Moho *Ps* and PpPs phases for both stations are very similar, which also proves the compatibility of both data sets. Using the *Ps* and PpPs arrival times to estimate the

Moho depth and V_p/V_s ratio, the uncertainties are mostly caused by the reading errors of the *Ps* and PpPs delay times. For each station, we perform 100 bootstrap realizations of the above mentioned procedures with the same number of P-RFs randomly selected from the original data set, to calculate the two standard deviations (2σ) of the mean value, which can be regarded as the rough estimation of the uncertainties in Moho depth and V_p/V_s ratio. In addition, an average crustal V_p of 6.2 km/s from a regional travel time tomography is used (Razi, Levin, Roecker, & Gilligan, 2014). To explore the uncertainties in Moho depth and V_p/V_s ratio resulting from the choice of average crustal V_p, we recalculate the Moho depths and V_p/V_s ratios of all the stations using average crustal V_p of 6.0 km/s and 6.5 km/s. The uncertainties generated by this analysis are less than ±4.0 km for the Moho depth and no more than ±0.01 for the V_p/V_s ratio. The prevailing H-κ stacking method does not provide reliable results at most stations, which can likely be attributed to the weak Moho multiples and the disturbance of intracrustal layers.

3.3. Depth Migration

To intuitively visualize the subsurface structures revealed by the receiver functions, we create linear depth sections by a common conversion points stacking technique (CCP) (Dueker & Sheehan, 1998; Kind et al., 2002; Ryberg & Weber, 2000), which is equivalent to depth migration and has been widely adopted in many studies around the world. Each depth profile is divided into grids with spacing of 2 km along the profile and 2 km in depth. The *Ps* (*Sp*) amplitudes of each receiver function are back projected to their spatial conversion points along the raypath. The velocity model used for the ray tracing is composed of a 80 km thick crust with an average V_p of 6.2 km/s and a V_p/V_s ratio of 1.732, underlain by the IASP91 mantle structure. All of the amplitudes are then stacked along the direction perpendicular to the profile within a width of 200 km to generate a vertical cross section, taking into account the piercing point distributions at depths of Moho and LAB. Finally, we perform the horizontal stacking within one Fresnel zone along the profile to produce a smoothed image for structural interpretation. The radius of one Fresnel zone is computed using $\sqrt{\frac{1}{2}\lambda h + \frac{1}{16}\lambda^2}$, where λ is the wavelength depending on the V_s and the dominant period of the signal, and h is the depth (Ryberg & Weber, 2000). At a depth of ~70 km, this lateral width is ~11 km for P-RF and ~23 km for S-RF.

To demonstrate the stability of CCP image features and assist the subsequent tectonic interpretations, we run 100 bootstrapping realizations of CCP stacking with a subset of 90% of total receiver function along each profile. Based on these realizations, we compute the number of the standard deviations in each grid of the CCP image along profiles X and Y (see supporting information, Figures S1 and S2). Given that the different numbers of P-RFs and S-RFs are used in CCP stacking, only the grids with amplitudes larger than two standard deviations for P-RF CCP image and 1.5 standard deviations for S-RF CCP image are considered as the robust observations.

There is no widely accepted velocity model available for our study area so far, so the depth errors in the CCP image mostly come from the deviations of our 1-D velocity model used from the actual structure of the Earth. Tests have proved that a 5% change in the average V_p or V_p/V_s ratio relative to the selected velocity model may account for ~3 km uncertainties in the Moho depth for the CCP stacking of P-RFs (Caldwell et al., 2013). On the other hand, the vertical resolution of receiver function can be determined by half of the wavelength of the *S* wave (Levin et al., 2016). The dominant periods of the P-RFs and S-RFs in our study are 1 s and 4 s, respectively, corresponding to maximum vertical resolutions at the Moho of 2 km for *Ps* and 8 km for *Sp* conversions assuming a lower crustal V_s of 4.0 km/s. Likewise, the errors in the LAB depth identified by CCP stacking of S-RFs are inferred to be about 9 km for a lithospheric mantle V_s of 4.5 km/s. We conclude that the uncertainties introduced by the selected velocity model are unlikely to significantly distort the pattern of the final CCP images.

4. Results and Discussion

4.1. Moho

Figures 4 and 5 present the stacked traces of the P-RFs at each station along lines X and Y, respectively. Each section is divided into two time windows, which encompass the Moho *Ps* (−5 to 15 s) and PpPs phases (15 to 45 s), respectively. Prior to stacking, zero-phase band-pass filters of 2–50 s and 4–50 s are applied to all P-RFs in the Moho *Ps* and PpPs phases windows, respectively. The Moho PpPs phase can be more reliably identified at lower frequency. In Figures 4 and 5, the Moho *Ps* phases with coherent positive amplitudes between 6.5 s

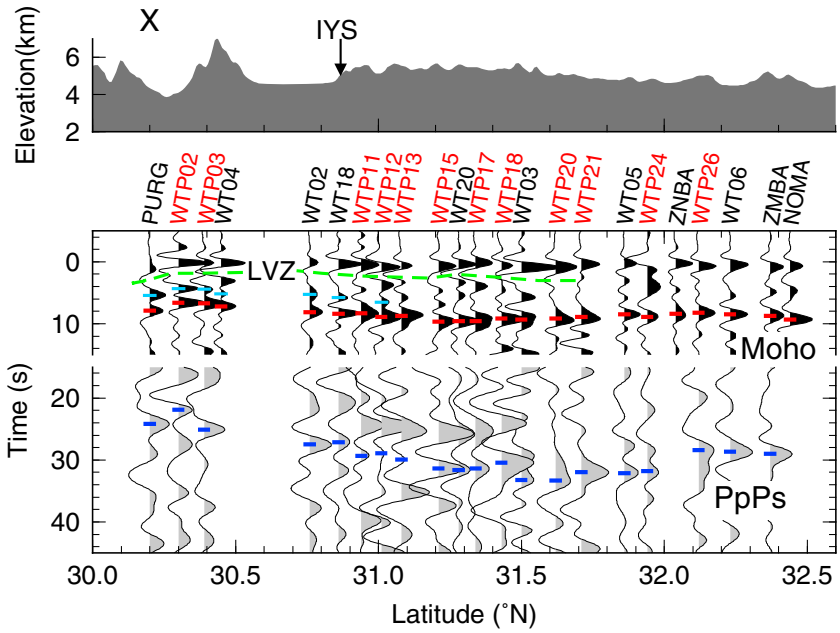

Figure 4. Stacked traces of all of the P-RFs at each station along section X after moveout corrections for *Ps* (top) and PpPs (bottom), respectively. The picked delay times of the Moho *Ps* and PpPs conversions are denoted by short red and blue lines, respectively. The short cyan lines indicate *Ps* conversions at an intracrustal interface. The green dashed line marks the top of the low-velocity zone (LVZ). The stations with names in red are from the ANTILOPE-1 project, and the other stations belong to the Y2 array. The topography along profile X is shown at the top of the figure.

and 10 s are clearly recognized along lines X and Y, while the positive pulses with significant amplitudes at ~1 s represent both the *Ps* conversions from a shallow sediment layer and the remaining *P* energy. At five stations (WT04, ZNBA, NOMA, WT08, and GARY), where no clear Moho PpPs phases can be reliably picked, we estimate the Moho depths using the *Ps* delay times and a V_p/V_s ratio of 1.732. In this case, the uncertainty in Moho depth has positive correlation with the Moho *Ps* time except the deviation between the real V_p/V_s ratio and 1.732 (Xu et al., 2010). The estimated Moho depths and uncertainties from all of the available stations are summarized in Table S1 in the supporting information.

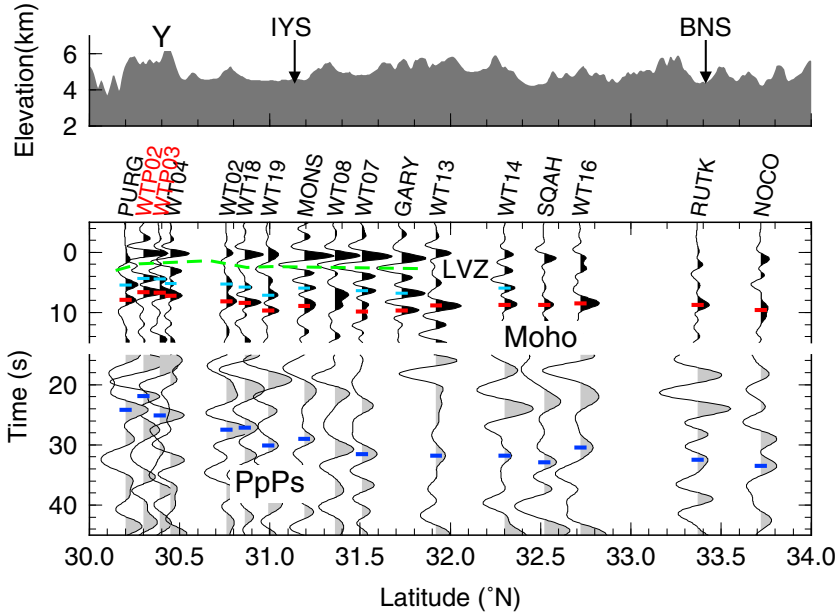

Figure 5. Same as Figure 3 but for section Y.

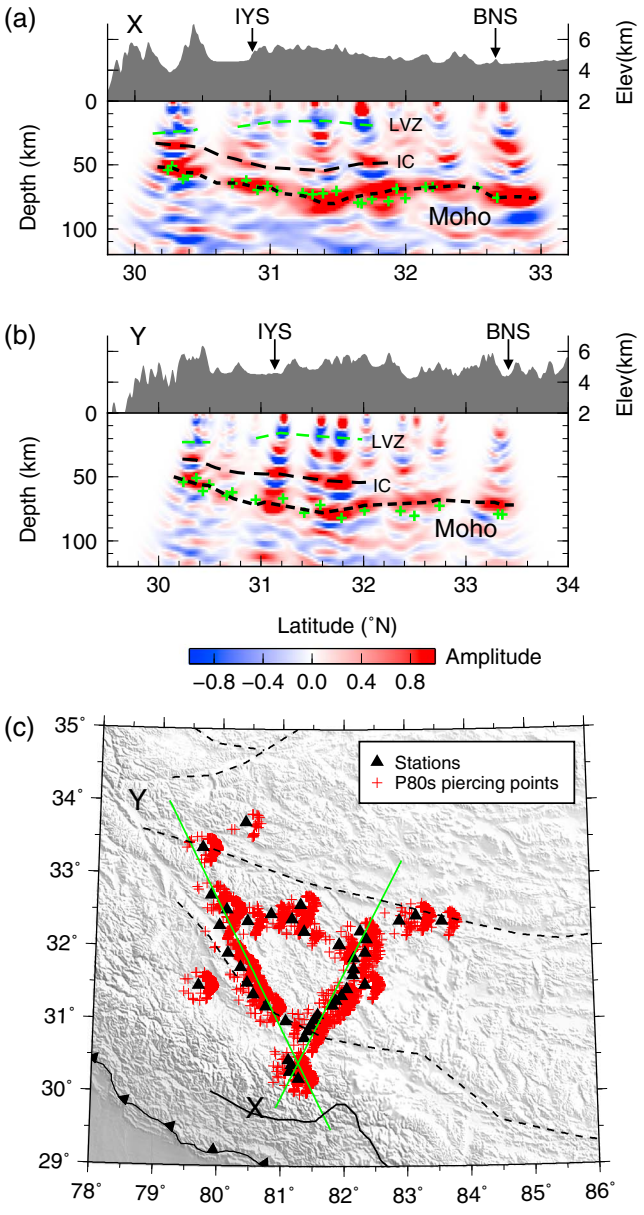

Figure 6. (a, b) CCP stacking images of P-RFs along profiles X and Y. Red (blue) colors represent positive (negative) amplitudes, which indicate increasing (decreasing) velocities downward. The green crosses illustrate the Moho depths derived in Figures 3 and 4 for comparison with the smooth Moho (black dashed line) in the P-RF images. The green and black dashed lines mark the intracrustal interface (IC) and the top of LVZ, respectively. (c) Map of *Ps* piercing points at 80 km depth (red pluses) along with the locations of the two CCP profiles.

We also construct P-RFs CCP stacking images along profiles X and Y (Figure 6). In both sections, the Moho can be clearly imaged by the strong positive signals, marked by the black dashed lines. We mark the Moho depths calculated by picking Moho *Ps* and PpPs delay times (Figures 4 and 5) onto the CCP stacking images (green crosses). The two types of Moho depth estimates agree well with each other at most places. Differences beneath some stations are resulted from the deviation of actual crustal V_p/V_s ratio from 1.732 in the model, used for the CPP stacking.

Our Moho depth estimates agree with the results derived from the joint inversion of the P-RF and group velocity at most stations of the Y2 array (Gilligan et al., 2015) with discrepancies of less than 5 km, which is within a reasonable range of uncertainty. However, at WT19, WT08, WT07, and GARY, our Moho depth estimates are 10–20 km deeper than those obtained by Gilligan et al. (2015). These stations are close to the IYS and the Karakoram Fault and have double positive pulses at the time where Moho arrival may appear. A possible explanation for these differences is that Gilligan et al. (2015) chose the phase at about 6.5 s as the Moho, while we believe that it marks the intracrustal discontinuity and pick the later phase as the Moho conversion, which has larger amplitude than the Moho signal, probably due to a gradual Moho velocity contrast. At some other stations, the differences in the Moho depths are less than 10 km and can be explained as being induced by different V_p/V_s ratios used in the two studies. We determined the V_p/V_p ratio from the receiver functions, while a fixed V_p/V_s ratio of 1.79 was used in Gilligan et al. (2015).

Along line X, the Moho deepens northward from ~55 km at 30.2°N south of the IYS to its deepest point of ~80 km at ~31.5°N beneath the central Lhasa terrane, shallows to ~67 km beneath northern the Lhasa terrane, and then deepens to ~75 km under the BNS. Along line Y, the Moho deepens across the IYS from ~55 km at ~30.2°N to the deepest location of ~82 km at ~31.7°N and then shallows to ~78 km beneath the northern Lhasa terrane. Therefore, it can be inferred that the Moho depth exhibits similar concave variations along the two lines, which resembles the previous observations from receiver functions farther east along the Hi-CLIMB, INDEPTH, and ANTILOPE-2 profiles (Kind et al., 2002; Nabelek et al., 2009; Xu et al., 2015) and to the west along TW-80 experiment at ~80°E (Zhang et al., 2014) and a profile at ~77°E (Rai et al., 2006).

The deepest Moho in our study region is located approximately 50 to 80 km north of the IYS, which is similar to that observed within tens of kilometers north of the IYS along the profiles mentioned above, except along a profile at ~92°E, where the Moho depth increases to ~70 km about 60 km south of the IYS and becomes horizontal until ~160 km north of the IYS (Shi et al., 2015). The continuity of the Moho across the IYS observed in this study could indicate that the Karakoram fault (KKF) does not cut through the crust, which is consistent with the analyses of a seismic reflection profile at 81.5°E showing that the KKF is confined to the upper crust at depths of less than 15 km (Gao et al., 2016). Our observation is in conflict with the interpretations of the TW-80 experiment, which suggested that small changes in the Moho depths mark zones of localized shear on the subvertical tectonic boundaries (Zhang et al., 2014).

4.2. Underthrusting of the Indian Crust

As shown in Figures 4–6, we observe another prominent positive conversion, approximately 20 km above the Moho. This intracrustal interface dips gently northward from ~35 km beneath the Tethyan Himalaya to ~55 km beneath the southern Lhasa terrane, which is referred to as the Moho doublet in the INDEPTH

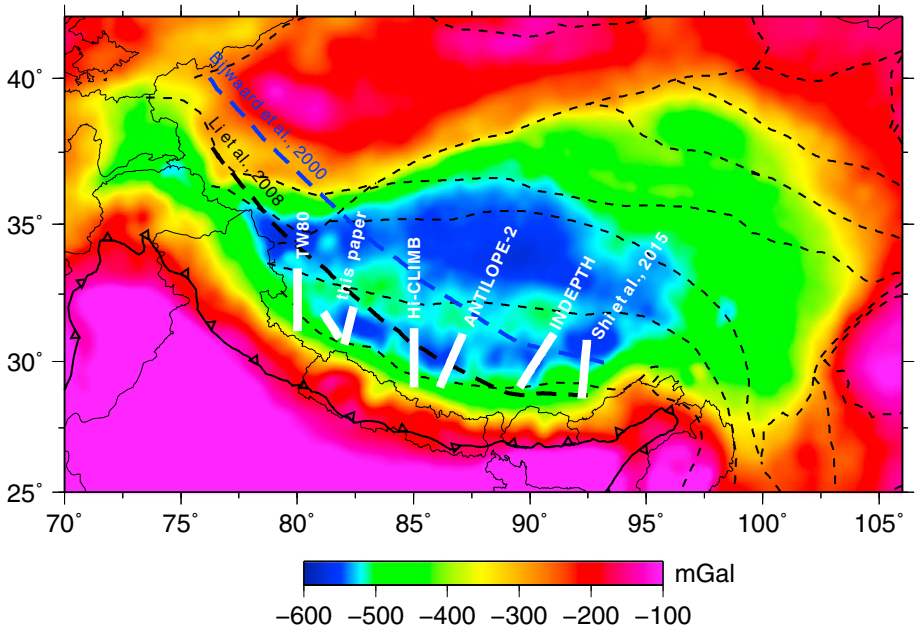

Figure 7. White lines denote the locations of the underthrusting Indian lower crust observed along several experiments in southern Tibet (Kind et al., 2002; Nabelek et al., 2009; Shi et al., 2015; Xu et al., 2015; Zhang et al., 2014). The background image is a smoothed Bouguer gravity model EGM2008 (Pavlis et al., 2012) with a spatial Gaussian filter of 150 km. The blue and black dashed lines from two different tomography results mark the front of the Indian lithospheric mantle (Bijwaard & Spakman, 2000; Kind & Yuan, 2010; Li et al., 2008).

section (Kind et al., 2002). This doublet represents the presence of a high-velocity layer above the Moho, which also has been observed along ANTILOPE-2 profile (Xu et al., 2015), Hi-CLIMB transect (Nabelek et al., 2009), TW-80 experiment at ~80°E (Zhang et al., 2014), and a profile at ~92°E (Shi et al., 2015). Gilligan et al. (2015) show some evidence of a small velocity increase in the velocity models and a clear conversion in the receiver functions above the Moho for some stations in the Lhasa terrane, which are consistent with the feature of this intracrustal discontinuity.

The intracrustal discontinuity south of the IYS coincides with the location of the MHT in an adjacent reflection profile at 81.5°E (Gao et al., 2016). The MHT is a strong midcrustal reflector beneath the Tethyan Himalaya that was first suggested by wide-angle seismic reflections at 90°E (Hirn et al., 1984) and was confirmed by the INDEPTH near-vertical reflection profile (Zhao et al., 1993). The MHT, with a ramp geometry beneath the Tethyan Himalaya, was identified either as a negative velocity contrast on the Hi-CLIMB receiver function section that was attributed to the presence of trapped fluid (Nabelek et al., 2009), or as an anisotropic shear zone along the HIMNT profile (Schulte-Pelkum et al., 2005). However, the MHT likely has different polarities in different regions due to different lithologies juxtaposed across this interface. It becomes a positive impedance contrast beneath the Tethyan Himalaya (Caldwell et al., 2013; Shi et al., 2015). Therefore, we tentatively link this positive intracrustal conversion to the MHT south of the surface exposition of IYS and interpret it as the top of the underplated Indian crust beneath the southern Lhasa terrane. This interpretation means that this intracrustal interface links the MHT to the top of the Indian lower crust and marks the upper boundary of the underthrusting Indian crust beneath the Himalaya and the southern Lhasa terrane. Along this interface, the Indian upper crust and sediments extrude southward, perhaps either by crustal-scale duplexing (Gao et al., 2016) or by channel flow (Beaumont et al., 2001). The fast Indian lower crust has attached to the base of the crust beneath the central Lhasa terrane (~32°N), whose front zone has thickened due to the obstruction of the stronger northern Lhasa terrane. In addition, evidence of high *P* wave velocity (Schulte-Pelkum et al., 2005), high density (Hetenyi et al., 2007), and low V_p/V_s ratios (Wittlinger et al., 2009) suggests that the fast Indian lower crust has acquired variable degrees of eclogitization beneath Tethyan Himalaya and the southern Lhasa terrane.

The underthrusting Indian lower crust has been observed in the southern Lhasa terrane along a number of N-S trending profiles, whose northern limit varies along strike from east to west (Kind et al., 2002; Nabelek

et al., 2009; Shi et al., 2015; Xu et al., 2015; Zhang et al., 2014). The Indian crustal underthrusting is widespread beneath the Lhasa terrane, has contributed to the crustal thickening, and results in the deepest Moho there. In Figure 7, we present these observations superposed on the Bouguer anomaly map derived from the gridded gravitational model EGM2008 (Pavlis et al., 2012). The Bouguer gravity data have been smoothed by a Gaussian filter with a width of 150 km. Two large-scale east-west stretching gravity lows are prominent in northern Tibet and in the southern Lhasa terrane. The two gravity anomalies have been separated by Pavlis et al. (2012) with low- and high-pass filters, respectively. The anomaly in northern Tibet has a much longer wavelength and may have more influence from mantle lithosphere, while the other anomaly in the southern Lhasa terrane has a shorter wavelength (much enhanced after a high-pass filter in Mishra et al. (2012)) and should receive more crustal contribution. As shown in Figure 7, there is a good agreement between the observed underthrusting Indian lower crust and the low Bouguer anomaly in the southern Lhasa terrane, which indicates a close connection between them. Jin et al. (1996) explained the Bouguer anomaly with a model of overlapping of Indian and Eurasian plates. However, regional tomography results indicate that the lateral heterogeneous Indian lithosphere extends to the IYS in western Tibet (Razi et al., 2016), to the BNS in central Tibet and to the JRS in eastern Tibet (Basuyau et al., 2013; Liang et al., 2016). These observations of the front of the Indian mantle lithosphere together with other different tomography results (Bijwaard & Spakman, 2000; Kind & Yuan, 2010; Li et al., 2008), as indicated by the two lines in Figure 7, do not match the geometry of the gravity low in the Lhasa terrane. So it seems that the gravity anomaly in the Lhasa terrane is not likely related to the plate geometry but to the underthrusting Indian lower crust causing the maximum crustal thickness under the Lhasa terrane.

4.3. Midcrustal Low-Velocity Zone

In Figure 6, a strong negative signal is identified beneath the Tethyan Himalaya and the southern Lhasa terrane with a data gap immediately south of the IYS. This interface has a south-dipping geometry from ~15–20 km beneath the southern Lhasa terrane to ~25 km beneath the Tethyan Himalaya and is generally considered as the top of a midcrustal LVZ. This LVZ is also clearly visible at the same location in the shear velocity section from the Y2 array (Gilligan et al., 2015; Razi, Levin, Roecker, & Huang, 2014) and is in agreement with similar observations along the ANTILOPE-2 profile in the central Lhasa terrane (Xu et al., 2015) and along INDEPTH reflection profiles (Brown et al., 1996; Nelson et al., 1996), receiver function images (Yuan et al., 1997), ambient noise tomography (Yang et al., 2012), and MT studies (Wei et al., 2001) in the eastern Lhasa terrane.

The formation of this midcrustal LVZ is related to the partial melting of the crust created by the joint effects of excess water and high crustal heat production (Wei et al., 2001). This water can be released either from the underthrusting sediments (Nabelek et al., 2009) or from the basal erosion of the overlying Tibetan crust during the Indian crust underthrusting. The high crustal heat production can be attributed to the high radioactivity in the overthickened Tibetan crust (Nelson et al., 1996) and shear heating from the plastic deformation (Hochstein & Regenauer-Lieb, 1998). So the south-dipping midcrustal LVZ is likely dominated by a temperature distribution and is expected to be warmer beneath the Lhasa terrane and colder toward the south of IYS. In addition, the combination of aqueous fluids and partial melting resulted from the crustal thickening can be responsible for the midcrustal LVZ (Li et al., 2003), whose properties coincide with a high-conductivity zone (Chen et al., 1996; Wei et al., 2001), highly attenuated crustal *Lg* waves (Reese et al., 1999), and some negative polarity bright spots discovered in INDPETH experiment (Brown et al., 1996).

The presence of the midcrustal LVZ seems to be widespread in southern Tibet along the strike, but the lateral continuity of the midcrustal LVZ has not been determined (Hetenyi et al., 2011). On the other hand, we could not directly infer the occurrence of channel flow according to the existence of the midcrustal LVZ, because the crustal viscosity coefficient, which is the crucial link between them, is unknown (Bendick & Flesch, 2007). The measurements of 3He/4He ratios in geothermal springs suggest that the KKF may have modified the channel flow extrusion of the Himalaya in southwestern Tibet (Klemperer et al., 2013). Therefore, we cannot determine whether the channel flow model is accurate or not in southern Tibet in this study. However, we infer that this midcrustal LVZ may form a decollement that decouples the thrust/fold structures of the upper crust from the shortening and underthrusting involved in the lower crust during the thickening of the Tibetan crust.

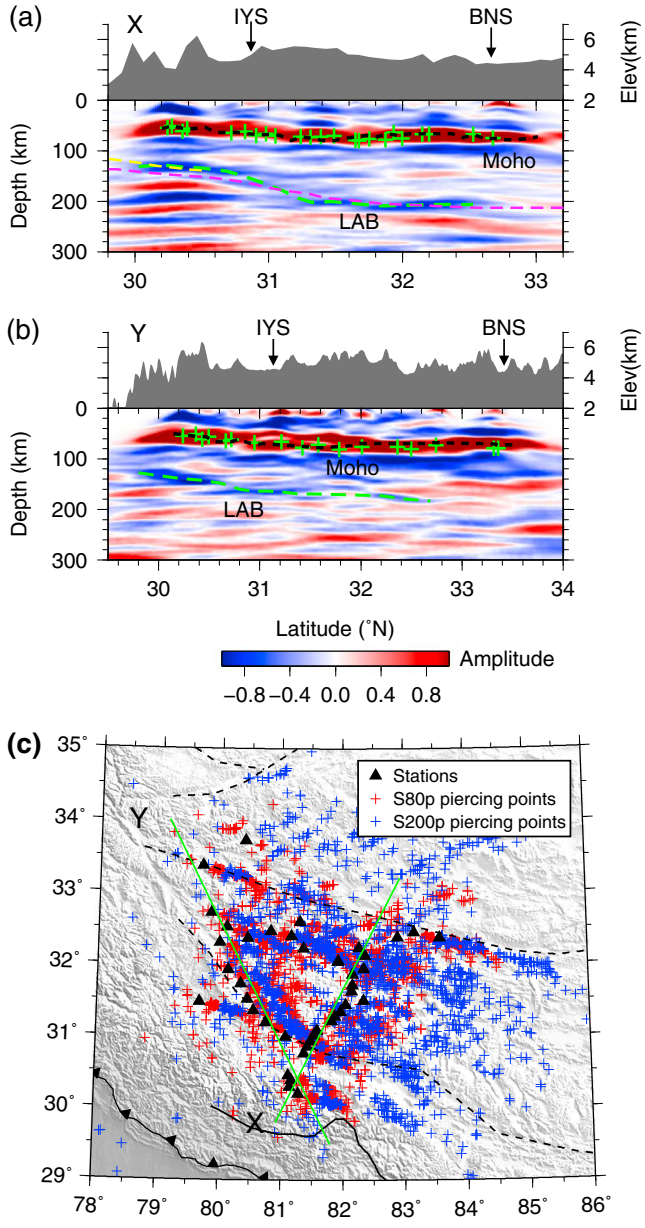

Figure 8. (a, b) Depth migrated images of the S-RFs along profiles X and Y. The Moho depths derived in the stacked traces from Figures 3 and 4 and CCP stacking images of the P-PRFs from Figure 5 are marked by the green crosses and black dashed lines, respectively. The recognized LABs in this research are denoted by the green dashed lines. The yellow and pink dashed lines (Figure 8a) mark the LABs from Kumar et al. (2013) and from Zhao et al. (2010) for reference, respectively. (c) Map of *Sp* piercing points at depths of 80 km (red pluses) and 200 km (blue pluses) along with the locations of the two CCP profiles.

4.4. LAB

To investigate the structure of the mantle lithosphere, we create S-RFs CCP stacking sections along profiles X and Y. As shown in Figure 8, the Moho is the most striking discontinuity along both profiles. The Moho depths are in good agreement with those determined by the P-RFs analysis, which also confirms the validity of our S-RFs images. The detection of the LAB conversions is less straightforward, because they are usually weak signals, often disturbed by noise. Here we refer to previous studies in the similar area (Kumar et al., 2013; Zhao et al., 2010) to detect coherent negative conversions below the Moho. Along line X, a negative discontinuity below the Moho with a ramp-flat geometry extends northward from ~130 km below the Tethyan Himalaya to 200 km about 30 km north of the IYS and remains nearly horizontal below the Lhasa terrane. This discontinuity can also be traced along profile Y, where it deepens northward from ~130 km below the Tethyan Himalaya to ~170 km near the IYS and becomes invisible beneath the northern part of the profile, where only about four stations are available for the CCP stacking. Given that most of the stations along profile Y are located along the IYS, we believe that the variations of this interface are consistent in the two profiles. Moreover, the more prominent pulses with the negative polarities immediately below the Moho probably are Moho sidelobes. Given that the amplitude deviation for each bin shown in Figure S2, we suggest that other strong negative features probably reflect noise or scattering associated with small-scale heterogeneities in the upper mantle.

Following Kumar et al. (2013), where the thickness of the Indian lithosphere is determined to be ~135 km near the MCT, we interpret this negative discontinuity as representing the Indian LAB beneath southern Tibet. Our observations of the Indian LAB have already been presented by Zhao et al. (2010). However, the S-RF images in this study are provided by many more stations and with more sophisticated CCP stacking technique. The shapes of the Indian LAB observed in our S-RF images correlate well with those from *P* wave tomographic images (Li et al., 2008) and low-resolution surface wave tomography (Maurya et al., 2016). In addition, synthetic tests have been performed to evaluate the robustness of our identified LABs. We calculate the synthetic S-RFs using the RAYSUM software based on the real-data distribution (Frederiksen & Bostock, 2000). Models contain a homogeneous crust and mantle lithosphere defined by the Moho and LAB indicated in Figures 6 and 8. Migrated images from synthetic S-RFs are conducted in the same processing steps as applied for the real data (see supporting information). The well-resolved LABs in synthetic images of profiles X and Y correlate well with that of the synthetic models designed by the real migrated images, which also justifies the reliability of our estimated LABs.

The geometry of the LAB suggests that the Indian lithosphere is underthrusting beneath the southern Tibet with ramp-flat geometry and has probably reached the JRS (Zhao et al., 2010). Since the Indian lithospheric mantle beneath the Himalaya is about 70 km thick (Kumar et al., 2013), we speculate that the Indian lithospheric mantle detaches from the lower crust just under the IYS (Figure 9). However, the top of the Indian lithospheric mantle is not identified in our migrated images, probably because the velocity contrast between the two plates is too small to be detected. The position where the detachment begins in our study is ~50 km south of where it was identified along the INDEPTH profile at ~90°E (Kosarev et al., 1999), and about ~50 km north of the proposed mantle suture at ~92°E (Shi et al., 2015); Nabelek et al. (2009) proposed a coupled underthrusting between the

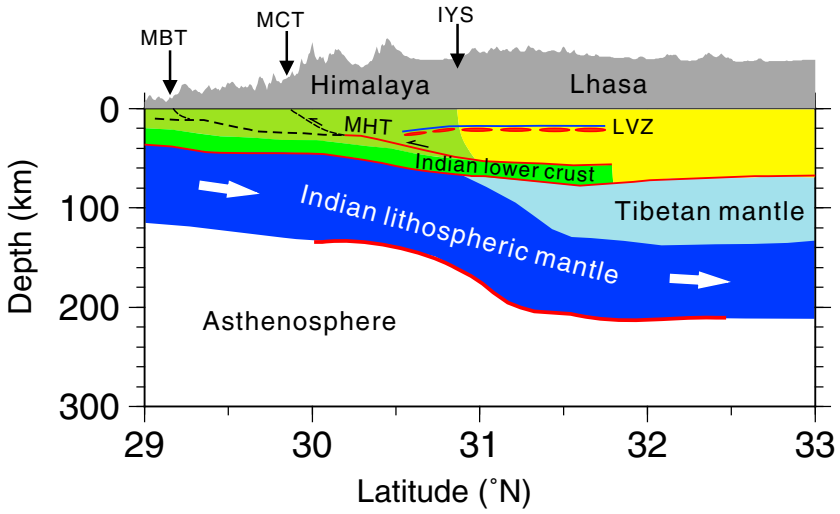

Figure 9. Sketch showing the configuration of the underthrusting Indian lithosphere. Our observations of the Moho, intracrustal interface, LVZ, and LAB are indicated by solid lines.

Indian crust and lithospheric mantle rather than a detachment along the Hi-CLIMB profile. In combination with the variations in the depth, shape, and northern borders of the Indian LAB along typical south-north sections as we discussed previously (Xu et al., 2011), these differences strongly support that the geometry of the underthrusting Indian lithosphere exhibits significant along strike variations (from west to east).

5. Conclusions

We investigate the lithospheric structure below western Tibet using the P-RF and S-RF techniques. The main conclusions are summarized by Figure 8 and are outlined as follows:

1. The Moho ranges in depth between 55 and 82 km with a concave shape and reaches the deepest location of 82 km north of the IYS.
2. An intracrustal interface at a depth of ~55 km beneath the southern Lhasa terrane probably connects the MTH south of the IYS and represents the upper boundary of the underthrusting Indian crust. Our preferred interpretation suggests that the eclogitized Indian lower crust has extended to the central Lhasa terrane (~32°N), which may have caused the Bouguer gravity low in the Lhasa terrane.
3. A midcrustal LVZ is observed at 15–25 km beneath the Tethyan Himalaya and the southern Lhasa terrane, which reflects the presence of partially molten crust. We propose that this LVZ reconciles the thrust/fold deformation of the upper crust from the shortening and underthrusting associated with the lower crust.
4. The LAB is observed at depths of 130–200 km, suggesting that the Indian lithospheric mantle is underthrusting beneath southern Tibet with ramp-flat shape and probably detaches from the lower crust just under the surface of IYS.

Acknowledgments
We sincerely thank the team of Steven Roecker and Vadim Levin for data collection and the IRIS DMC for making the Y2 data available. All the RFs computed from ANTILOPE-1 in this study are available through the Third Pole Environment Database at the Institute of Tibetan Plateau Research, Chinese Academy of Sciences (http://dx.doi.org/10.11888/Geophys.tpe.249474.file). Constructive comments from the Editors and two anonymous reviewers significantly improve the manuscript. This research is supported by the National Natural Science Foundation of China (41474066), Major Program of National Natural Science Foundation of China (41490611), and Strategic Priority Research Program (B) of the Chinese Academy of Sciences (XDB03010702). The Seismic Handler software and the Generic Mapping Tools (GMT) (Wessel & Smith, 1995) are used to process the waveform data and plot the figures, respectively.

References

Basuyau, C., Diament, M., Tiberi, C., Hetenyi, G., Vergne, J., & Peyrefitte, A. (2013). Joint inversion of teleseismic and GOCE gravity data: Application to the Himalayas. *Geophysical Journal International*, *193*(1), 149–160. https://doi.org/10.1093/gji/ggs110

Beaumont, C., Jamieson, R. A., Nguyen, M. H., & Lee, B. (2001). Himalayan tectonics explained by extrusion of a low-viscosity crustal channel coupled to focused surface denudation. *Nature*, *414*(6865), 738–742. https://doi.org/10.1038/414738a

Bendick, R., & Flesch, L. (2007). Reconciling lithospheric deformation and lower crustal flow beneath central Tibet. *Geology*, *35*(10), 895–898. https://doi.org/10.1130/G23714a.1

Bijwaard, H., & Spakman, W. (2000). Non-linear global *P*-wave tomography by iterated linearized inversion. *Geophysical Journal International*, *141*(1), 71–82. https://doi.org/10.1046/j.1365-246X.2000.00053.x

Brown, L. D., Zhao, W. J., Nelson, D. K., Hauck, M., Alsdorf, D., Ross, A., … Chen, J. K. (1996). Bright spots, structure, and magmatism in southern Tibet from INDEPTH seismic reflection profiling. *Science*, *274*(5293), 1688–1690. https://doi.org/10.1126/science.274.5293.1688

Caldwell, W. B., Klemperer, S. L., Lawrence, J. F., Rai, S. S., & Ashish (2013). Characterizing the Main Himalayan Thrust in the Garhwal Himalaya, India with receiver function CCP stacking. *Earth and Planetary Science Letters*, *367*, 15–27. https://doi.org/10.1016/j.epsl.2013.02.009

Chen, L. H., Booker, J. R., Jones, A. G., Wu, N., Unsworth, M. J., Wei, W. B., & Tan, H. D. (1996). Electrically conductive crust in southern Tibet from INDEPTH magnetotelluric surveying. *Science*, *274*(5293), 1694–1696. https://doi.org/10.1126/science.274.5293.1694

DeCelles, P. G., Robinson, D. M., & Zandt, G. (2002). Implications of shortening in the Himalayan fold-thrust belt for uplift of the Tibetan Plateau. *Tectonics*, *21*(6), 12-1–12-25. https://doi.org/10.1029/2001TC001322

Ding, L., Kapp, P., & Wan, X. Q. (2005). Paleocene-Eocene record of ophiolite obduction and initial India-Asia collision, south central Tibet. *Tectonics*, *24*(3), TC3001. https://doi.org/10.1029/2004TC001729

Dueker, K. G., & Sheehan, A. F. (1998). Mantle discontinuity structure beneath the Colorado Rocky Mountains and High Plains. *Journal of Geophysical Research*, *103*(B4), 7153–7169. https://doi.org/10.1029/97JB03509

Frederiksen, A. W., & Bostock, M. G. (2000). Modelling teleseismic waves in dipping anisotropic structures. *Geophysical Journal International*, *141*(2), 401–412. https://doi.org/10.1046/j.1365-246x.2000.00090.x

Gao, R., Lu, Z. W., Klemperer, L., Wang, H. Y., Dong, S. W., Li, W. H., & Li, H. Q. (2016). Crustal-scale duplexing beneath the Yarlung Zangbo suture in the western Himalaya. *Nature Geoscience*, *9*(7), 555–560. https://doi.org/10.1038/NGEO2730

Gilligan, A., Priestley, K. F., Roecker, S. W., Levin, V., & Rai, S. S. (2015). The crustal structure of the western Himalayas and Tibet. *Journal of Geophysical Research: Solid Earth*, *120*, 3946–3964. https://doi.org/10.1002/2015JB011891

Hetenyi, G., Cattin, R., Brunet, F., Bollinger, L., Vergne, J., Nabelek, J., & Diament, M. (2007). Density distribution of the India plate beneath the Tibetan Plateau: Geophysical and petrological constraints on the kinetics of lower-crustal eclogitization. *Earth and Planetary Science Letters*, *264*(1-2), 226–244. https://doi.org/10.1016/j.epst.2007.09.036

Hetenyi, G., Vergne, J., Bollinger, L., & Cattin, R. (2011). Discontinuous low-velocity zones in southern Tibet question the viability of the channel flow model. *Geological Society of London, Special Publication*, *353*(1), 99–108. https://doi.org/10.1144/SP353.6

Hirn, A., Nercessian, A., Sapin, M., Jobert, G., Xu, Z. X., Gao, E. Y., … Teng, J. W. (1984). Lhasa block and bordering sutures—A continuation of a 500-km Moho traverse through Tibet. *Nature*, *307*(5946), 25–27. https://doi.org/10.1038/307025a0

Hochstein, M. P., & Regenauer-Lieb, K. (1998). Heat generation associated with collision of two plates: The Himalayan geothermal belt. *Journal of Volcanology and Geothermal Research*, *83*(1-2), 75–92. https://doi.org/10.1016/S0377-0273(98)00018-3

Jin, Y., McNutt, M. K., & Zhu, Y. S. (1996). Mapping the descent of Indian and Eurasian plates beneath the Tibetan Plateau from gravity anomalies. *Journal of Geophysical Research*, *101*(B5), 11,275–11,290. https://doi.org/10.1029/96JB00531

Kind, R., & Yuan, X. H. (2010). Seismic images of the biggest crash on Earth. *Science*, *329*(5998), 1479–1480. https://doi.org/10.1126/science.1191620

Kind, R., Yuan, X. H., & Kumar, P. (2012). Seismic receiver functions and the lithosphere-asthenosphere boundary. *Tectonophysics*, *536-537*, 25–43. https://doi.org/10.1016/j.tecto.2012.03.005

Kind, R., Yuan, X., Saul, J., Nelson, D., Sobolev, S. V., Mechie, J., … Jiang, M. (2002). Seismic images of crust and upper mantle beneath Tibet: Evidence for Eurasian plate subduction. *Science*, *298*(5596), 1219–1221. https://doi.org/10.1126/science.1078115

Klemperer, S. L., Kennedy, B. M., Sastry, S. R., Makovsky, Y., Harinarayana, T., & Leech, M. L. (2013). Mantle fluids in the Karakoram fault: Helium isotope evidence. *Earth and Planetary Science Letters*, *366*, 59–70. https://doi.org/10.1016/j.eps1.2013.01.013

Kosarev, G., Kind, R., Sobolev, S. V., Yuan, X., Hanka, W., & Oreshin, S. (1999). Seismic evidence for a detached Indian lithospheric mantle beneath Tibet. *Science*, *283*(5406), 1306–1309. https://doi.org/10.1126/science.283.5406.1306

Kumar, P., & Kawakatsu, H. (2011). Imaging the seismic lithosphere-asthenosphere boundary of the oceanic plate. *Geochemistry, Geophysics, Geosystems*, *12*(1), Q01006. https://doi.org/10.1029/2010GC003358

Kumar, P., Kumar, M. R., Srijayanthi, G., Arora, K., Srinagesh, D., Chadha, R. K., & Sen, M. K. (2013). Imaging the lithosphere-asthenosphere boundary of the Indian plate using converted wave techniques. *Journal of Geophysical Research: Solid Earth*, *118*, 5307–5319. https://doi.org/10.1002/jgrb.50366

Levin, V., VanTongeren, J. A., & Servali, A. (2016). How sharp is the sharp Archean Moho? Example from eastern Superior Province. *Geophysical Research Letters*, *43*(5), 1928–1933. https://doi.org/10.1002/2016GL067729

Li, S. H., Unsworth, M. J., Booker, J. R., Wei, W. B., Tan, H. D., & Jones, A. G. (2003). Partial melt or aqueous fluid in the mid-crust of Southern Tibet? Constraints from INDEPTH magnetotelluric data. *Geophysical Journal International*, *153*(2), 289–304. https://doi.org/10.1046/j.1365-246X.2003.01850.x

Li, C., Van der Hilst, R. D., Meltzer, A. S., & Engdahl, E. R. (2008). Subduction of the Indian lithosphere beneath the Tibetan Plateau and Burma. *Earth and Planetary Science Letters*, *274*(1-2), 157–168. https://doi.org/10.1016/j.epsl.2008.07.016

Li, X. Q., & Yuan, X. H. (2003). Receiver functions in northeast China—Implications for slab penetration into the lower mantle in northwest Pacific subduction zone. *Earth and Planetary Science Letters*, *216*(4), 679–691. https://doi.org/10.1016/S0012-821x(03)00555-7

Liang, X. F., Chen, Y., Tian, X. B., Chen, Y. J., Ni, J., Gallegos, A., … Teng, J. W. (2016). 3D imaging of subducting and fragmenting Indian continental lithosphere beneath southern and central Tibet using body-wave finite-frequency tomography. *Earth and Planetary Science Letters*, *443*, 162–175. https://doi.org/10.1016/j.epsl.2016.03.029

Maurya, S., Montagner, J. P., Kumar, M. R., Stutzmann, E., Kiselev, S., Burgos, G., … Srinagesh, D. (2016). Imaging the lithospheric structure beneath the Indian continent. *Journal of Geophysical Research: Solid Earth*, *121*, 7450–7468. https://doi.org/10.1002/2016JB012948

Mishra, D. C., Kumar, M. R., & Arora, K. (2012). Long wavelength satellite gravity and geoid anomalies over Himalaya, and Tibet: Lithospheric structures and seismotectonics of deep focus earthquakes of Hindu Kush - Pamir and Burmese arc. *Journal of Asian Earth Sciences*, *48*, 93–110. https://doi.org/10.1016/j.jseaes.2011.12.003

Nabelek, J., Hetenyi, G., Vergne, J., Sapkota, S., Kafle, B., Jiang, M., … the Hi-CLIMB Team (2009). Underplating in the Himalaya-Tibet collision zone revealed by the Hi-CLIMB experiment. *Science*, *325*(5946), 1371–1374. https://doi.org/10.1126/science.1167719

Nelson, K. D., Zhao, W. J., Brown, L. D., Kuo, J., Che, J. K., Liu, X. W., … Edwards, M. (1996). Partially molten middle crust beneath southern Tibet: Synthesis of project INDEPTH results. *Science*, *274*(5293), 1684–1688. https://doi.org/10.1126/science.274.5293.1684

Pavlis, N. K., Holmes, S. A., Kenyon, S. C., & Factor, J. K. (2012). The development and evaluation of the Earth Gravitational Model 2008 (EGM2008). *Journal of Geophysical Research*, *117*(B4), B04406. https://doi.org/10.1029/2011JB008916

Rai, S. S., Priestley, K., Gaur, V. K., Mitra, S., Singh, M. P., & Searle, M. (2006). Configuration of the Indian Moho beneath the NW Himalaya and Ladakh. *Geophysical Research Letters*, *33*(15), L15308. https://doi.org/10.1029/2006GL026076

Razi, A. S., Levin, V., Roecker, S. W., & Gilligan, A. (2014). Crustal structure beneath western Tibet: Evidence from receiver functions and newly constrained *P* and *S*-wave velocity models. Paper presented at the 2014 AGU Fall Meeting, San Francisco. Retrieved from https://agu.confex.com/agu/fm14/webprogram/Paper17800.html

Razi, A. S., Levin, V., Roecker, S. W., & Huang, G. C. D. (2014). Crustal and uppermost mantle structure beneath western Tibet using seismic traveltime tomography. *Geochemistry, Geophysics, Geosystems*, *15*(2), 434–452. https://doi.org/10.1002/2013GC005143

Razi, A. S., Roecker, S. W., & Levin, V. (2016). The fate of the Indian lithosphere beneath western Tibet: Upper mantle elastic wave speed structure from a joint teleseismic and regional body wave tomographic study. *Physics of the Earth and Planetary Interiors*, *251*, 11–23. https://doi.org/10.1016/j.pepi.2015.12.001

Reese, C. C., Rapine, R. R., & Ni, J. F. (1999). Lateral variation of Pn and Lg attenuation at the CDSN station LSA. *Bulletin of the Seismological Society of America*, *89*(1), 325–330.

Ryberg, T., & Weber, M. (2000). Receiver function arrays: A reflection seismic approach. *Geophysical Journal International*, *141*(1), 1–11. https://doi.org/10.1046/j.1365-246X.2000.00077.x

Schulte-Pelkum, V., Monsalve, G., Sheehan, A., Pandey, M. R., Sapkota, S., Bilham, R., & Wu, F. (2005). Imaging the Indian subcontinent beneath the Himalaya. *Nature*, *435*(7046), 1222–1225. https://doi.org/10.1038/Nature03678

Shi, D. N., Wu, Z. H., Klemperer, S. L., Zhao, W. J., Xue, G. Q., & Su, H. P. (2015). Receiver function imaging of crustal suture, steep subduction, and mantle wedge in the eastern India-Tibet continental collision zone. *Earth and Planetary Science Letters*, *414*, 6–15. https://doi.org/10.1016/j.epsl.2014.12.055

van Hinsbergen, D. J. J., Kapp, P., Dupont-Nivet, G., Lippert, P. C., DeCelles, P. G., & Torsvik, T. H. (2011). Restoration of Cenozoic deformation in Asia and the size of Greater India. *Tectonics*, *30*(5), TC5003. https://doi.org/10.1029/2011TC002908

Wei, W. B., Unsworth, M., Jones, A., Booker, J., Tan, H. D., Nelson, D., … Roberts, B. (2001). Detection of widespread fluids in the Tibetan crust by magnetotelluric studies. *Science*, *292*(5517), 716–719. https://doi.org/10.1126/science.1010580

Wessel, P., & Smith, W. H. F. (1995). New version of the Generic Mapping Tools released. *Eos, Transactions of the American Geophysical Union*, *76*(33), 329–329. https://doi.org/10.1029/95EO00198

Wittlinger, G., Farra, V., Hetenyi, G., Vergne, J., & Nabelek, J. (2009). Seismic velocities in southern Tibet lower crust: A receiver function approach for eclogite detection. *Geophysical Journal International*, *177*(3), 1037–1049. https://doi.org/10.1111/j.1365-246X.2008.04084.x

Wittlinger, G., Vergne, J., Tapponnier, P., Farra, V., Poupinet, G., Jiang, M., … Paul, A. (2004). Teleseismic imaging of subducting lithosphere and Moho offsets beneath western Tibet. *Earth and Planetary Science Letters*, *221*(1-4), 117–130. https://doi.org/10.1016/S0012-821x(03)00723-4

Xu, Z. J., Song, X. D., & Zhu, L. P. (2013). Crustal and uppermost mantle S velocity structure under Hi-CLIMB seismic array in central Tibetan Plateau from joint inversion of surface wave dispersion and receiver function data. *Tectonophysics*, *584*, 209–220. https://doi.org/10.1016/j.tecto.2012.08.024

Xu, Q., Zhao, J. M., Cui, Z. X., Pei, S. P., & Liu, H. B. (2010). Moho offset beneath the central Bangong-Nujiang suture of Tibetan Plateau. *Chinese Science Bulletin*, *55*(7), 607–613. https://doi.org/10.1007/s11434-009-0387-9

Xu, Q., Zhao, J. M., Pei, S. P., & Liu, H. B. (2011). The lithosphere-asthenosphere boundary revealed by S-receiver functions from the Hi-CLIMB experiment. *Geophysical Journal International*, *187*(1), 414–420. https://doi.org/10.1111/j.1365-246X.2011.05154.x

Xu, Q., Zhao, J. M., Yuan, X. H., Liu, H. B., & Pei, S. P. (2015). Mapping crustal structure beneath southern Tibet: Seismic evidence for continental crustal underthrusting. *Gondwana Research*, *27*(4), 1487–1493. https://doi.org/10.1016/j.gr.2014.01.006

Yang, Y. J., Ritzwoller, M. H., Zheng, Y., Shen, W. S., Levshin, A. L., & Xie, Z. J. (2012). A synoptic view of the distribution and connectivity of the mid-crustal low velocity zone beneath Tibet. *Journal of Geophysical Research*, *117*(B4), B04303. https://doi.org/10.1029/2011JB008810

Yin, A., & Harrison, T. M. (2000). Geologic evolution of the Himalayan-Tibetan orogen. *Annual Review of Earth and Planetary Sciences*, *28*(1), 211–280. https://doi.org/10.1146/annurev.earth.28.1.211

Yuan, X. H., Kind, R., Li, X. Q., & Wang, R. J. (2006). The S receiver functions: Synthetics and data example. *Geophysical Journal International*, *165*(2), 555–564. https://doi.org/10.1111/j.1365-246X.2006.02885.x

Yuan, X. H., Ni, J., Kind, R., Mechie, J., & Sandvol, E. (1997). Lithospheric and upper mantle structure of southern Tibet from a seismological passive source experiment. *Journal of Geophysical Research*, *102*(B12), 27,491–27,500. https://doi.org/10.1029/97JB02379

Yuan, X., Sobolev, S. V., & Kind, R. (2002). Moho topography in the central Andes and its geodynamic implications. *Earth and Planetary Science Letters*, *199*(3-4), 389–402. https://doi.org/10.1016/S0012-821x(02)00589-7

Zhang, Z. J., Wang, Y. H., Houseman, G. A., Xu, T., Wu, Z. B., Yuan, X. H., … Teng, J. W. (2014). The Moho beneath western Tibet: Shear zones and eclogitization in the lower crust. *Earth and Planetary Science Letters*, *408*, 370–377. https://doi.org/10.1016/j.epsl.2014.10.022

Zhao, W. J., Nelson, K. D., & Team, P. I. (1993). Deep seismic-reflection evidence for continental underthrusting beneath southern Tibet. *Nature*, *366*(6455), 557–559. https://doi.org/10.1038/366557a0

Zhao, J. M., Yuan, X. H., Liu, H. B., Kumar, P., Pei, S. P., Kind, R., … Wang, W. (2010). The boundary between the Indian and Asian tectonic plates below Tibet. *Proceedings of the National Academy of Sciences of the United States of America*, *107*(25), 11,229–11,233. https://doi.org/10.1073/pnas.1001921107

Zhao, J. M., Zhao, D. P., Zhang, H., Liu, H. B., Huang, Y., Cheng, H. G., & Wang, W. (2014). *P*-wave tomography and dynamics of the crust and upper mantle beneath western Tibet. *Gondwana Research*, *25*(4), 1690–1699. https://doi.org/10.1016/j.gr.2013.06.020